AIAA JOURNAL
Vol. 35, No. 7, July 1997

# High-Resolution Finite Volume Computation of Turbulent Transonic Flow Past Airfoils

Y. T. Jiang* and M. Damodaran†
*Nanyang Technological University, 639798 Singapore*
and
K. H. Lee‡
*Singapore Technologies Aerospace Ltd., 539938 Singapore*

**The objective is to develop a high-resolution numerical scheme for calculating turbulent transonic flows past airfoils. The numerical scheme essentially combines a multigrid explicit finite volume time-marching scheme with a convective upwind split pressure (CUSP) scheme for controlling artificial dissipation, and convergence rate is further enhanced by using local time stepping and implicit residual smoothing. One- and two-equation turbulence models are incorporated into the numerical scheme to assess the ability of various turbulence models in the prediction of turbulent transonic flow over airfoils within the framework of the CUSP formulation of artificial dissipation. An implicit, factored, upwind-biased numerical scheme is used for the integration of the turbulence field equations. Transonic viscous flows around the RAE-2822 airfoil are computed using this scheme. The results show reasonably good agreement with existing experimental data and an improved resolution of transonic viscous flows.**

## I. Introduction

THE structure of turbulent transonic flow around an airfoil is complex because of the presence of shock waves and viscous layers. When one computes this flowfield numerically, it is important to establish a high-resolution algorithm for the solution of turbulent transonic flows so as to improve the numerical prediction capabilities of the algorithm. Whereas a variety of efficient numerical solution procedures have been proposed for the solution of Navier–Stokes equations, the focus of this work is on explicit finite volume numerical schemes that require an explicit addition of artificial dissipative terms to ensure numerical stability and to resolve discontinuities and shear layers in the flowfield. The introduction of numerical dissipation could lead to the contamination of the physical dissipation and excessive smearing of shock waves. All of these affect the accuracy of the solution of viscous flow problems. Hence, there is a need to control the amount of artificial dissipation without affecting numerical stability. One approach is to reduce the artificial dissipation through the use of the velocity scaling of the artificial dissipation such as Kunz[1] and Varma and Caughey[2] or of the matrix-value dissipation of Turkel and Vatsa.[3] Although the matrix-valued dissipation produces better resolution of flow features than the scalar dissipation model does, it is not optimal.

Jameson[4] has proposed a unified theory of nonoscillatory finite volume schemes based on the local extremum diminishing principle, which leads to a new formulation of the convective upwind split pressure (CUSP) scheme that supports single-point shock capturing of stationary shocks. The CUSP scheme introduces a minimum amount of numerical dissipation as the Mach number approaches zero. Therefore, it is also appropriate for viscous flow calculations. Tatsumi et al.[5] have applied the CUSP scheme to solve turbulent transonic flow problems and have demonstrated improved resolution of viscous layers as well as maintaining single-point shock capturing characteristics. In the present work, the CUSP scheme has been implemented within the finite volume numerical scheme and has been explored with a variety of turbulence models, such as one-equation and two-equation turbulence models to develop a more general high-resolution procedure for turbulent transonic flow problems.

For turbulent flow calculations, the turbulence transport equations and mean flow equations may be solved in a coupled or a decoupled manner. Although the coupled approach gives a single system of equations, which simultaneously govern the mean flow and the turbulence properties, it is noted by Kunz[1] that there is no specific advantage to be gained numerically in terms of either convergence rate or accuracy. In view of this, a decoupled approach allows one to use different numerical schemes to integrate the mean flow equations and the turbulence transport equations thereby enabling one to investigate different turbulence models. The mean flow equations are integrated in time using turbulence quantities frozen from the last time step. In this work, the decoupled approach is used to integrate the turbulence transport equations in time using frozen mean flow properties. The CUSP scheme[6] is incorporated in the work of Damodaran and Lee,[7] which uses a finite volume multistage cell-centered explicit time-marching scheme to integrate the Favre-averaged Navier–Stokes equations. Because the presence of source terms in the turbulence transport equations imposes a further time step restriction, the implicit factored alternating direction implicit (ADI) scheme is used for solving the turbulence transport equations to alleviate the problem.

## II. Governing Equations

For compressible turbulent flows, the density weighted averaging suggested by Favre[8,9] is helpful in simplifying the formulation of the mean flow equations. The Favre averaging is a hybrid averaged method that uses density weighted averaging on all fluid properties except pressure and density on which an ensemble (or time) averaging is used. With the use of the eddy viscosity model in modeling the Reynolds stresses and turbulent heat flux, the nondimensional conservative form of Favre-averaged Navier–Stokes equations in two dimensions is written as

$$\frac{\partial \langle \boldsymbol{U} \rangle}{\partial t} + \frac{\partial \langle \boldsymbol{F} \rangle}{\partial x} + \frac{\partial \langle \boldsymbol{G} \rangle}{\partial y} = \frac{\overline{\gamma} M_\infty}{\sqrt{Re_L}} \left( \frac{\partial \langle \boldsymbol{R} \rangle}{\partial x} + \frac{\partial \langle \boldsymbol{S} \rangle}{\partial y} \right) \tag{1}$$

Here

$$\langle \boldsymbol{U} \rangle = (\langle \rho \rangle, \langle \rho \rangle \tilde{u}, \langle \rho \rangle \tilde{v}, \langle \rho \rangle \tilde{e})^T$$

$$\langle \boldsymbol{F} \rangle = [\langle \rho \rangle \tilde{u}, \langle \rho \rangle \tilde{u}^2 + \langle p \rangle, \langle p \rangle \tilde{u}\tilde{v}, \tilde{u}(\langle \rho \rangle \tilde{e} + \langle p \rangle)]^T$$

$$\langle \boldsymbol{G} \rangle = [\langle \rho \rangle \tilde{v}, \langle \rho \rangle \tilde{u}\tilde{v}, (\langle \rho \rangle \tilde{v}^2 + \langle p \rangle), \tilde{v}(\langle \rho \rangle \tilde{e} + \langle p \rangle)]^T$$

Received June 4, 1996; presented as Paper 96-2377 at the AIAA 14th Applied Aerodynamics Conference, New Orleans, LA, June 17–20, 1996; revision received Dec. 10, 1996; accepted for publication Jan. 21, 1997. 

*Postdoctoral Fellow, School of Mechanical and Production Engineering. Member AIAA.
†Senior Lecturer, School of Mechanical and Production Engineering. Senior Member AIAA.
‡Senior Engineer, Engineering Development Center. Member AIAA.

$$\langle \boldsymbol{R} \rangle = \left( 0,\ \tilde{\sigma}_{xx},\ \tilde{\sigma}_{xy},\ \tilde{u}\tilde{\sigma}_{xx} + \tilde{v}\tilde{\sigma}_{xy} + \kappa_\tau \frac{\partial \tilde{T}}{\partial x} \right)^T$$

$$\langle \boldsymbol{S} \rangle = \left( 0,\ \tilde{\sigma}_{xy},\ \tilde{\sigma}_{yy},\ \tilde{u}\tilde{\sigma}_{xy} + \tilde{v}\tilde{\sigma}_{yy} + \kappa_\tau \frac{\partial \tilde{T}}{\partial y} \right)^T$$

and the equation of state for a perfect gas is given by

$$\langle p \rangle = (\gamma - 1)\langle \rho \rangle \left[ \tilde{e} - \frac{\tilde{u}^2 + \tilde{v}^2}{2} \right] \tag{2}$$

where $\tilde{\sigma}_{xx}$, $\tilde{\sigma}_{xy}$, and $\tilde{\sigma}_{yy}$ are the stress terms, $\tilde{\sigma}_{xx} = 2\tilde{\mu}_e \tilde{u}_x - 2\tilde{\mu}_e (\tilde{u}_x + \tilde{v}_y)/3$, $\tilde{\sigma}_{xy} = \tilde{\mu}_e (\tilde{u}_y + \tilde{v}_x)$, and $\tilde{\sigma}_{yy} = 2\tilde{\mu}_e \tilde{v}_y - 2\tilde{\mu}_e (\tilde{u}_x + \tilde{v}_y)/3$. Also, $\kappa_\tau$ is the coefficient of thermal conductivity, $\kappa_\tau = (\tilde{\mu}/p_r)_e (\gamma - 1) M_\infty^2$.

In these equations, the angle brackets $\langle\,\rangle$ represent an ensemble-averaged quantity and the tilde ($\tilde{}$) defines a density weighted averaged quantity. Also, $\rho$, $u$, $v$, $e$, $p$, and $T$ represent the density, $x$- and $y$-velocity components, total energy, pressure, and the temperature, respectively. $Re_L$ is the reference Reynolds number based on the airfoil chord length $L$, $M_\infty$ is the freestream Mach number, and $\gamma$ is the ratio of specific heats of the fluid, taken as 1.4. The effective thermal conductivity $(\tilde{\mu}/p_r)_e = (\tilde{\mu}/p_r) + (\tilde{\mu}/p_r)_t$, where $p_r$ and $p_{r_t}$ are the laminar and turbulent Prandtl number taken as 0.72 and 0.9, respectively. The effective viscosity $\tilde{\mu}_e = \tilde{\mu} + \tilde{\mu}_t$, where the molecular viscosity $\tilde{\mu}$ is obtained by the power law $\tilde{\mu} = \tilde{T}^n$ with $n = 0.72$, and the turbulent viscosity $\tilde{\mu}_t$ is determined by a suitable turbulence model.

## III. Turbulence Models

In the present work, one-equation turbulence models of Baldwin–Barth[10] (B–B) and Spalart–Allmaras[11] (S–A) and the two-equation Chien's low Reynolds number $k$–$\epsilon$ model[12] (CH) are implemented to compute turbulence effects on the mean flow equations for turbulent transonic flow past airfoils. As these models account for near-wall viscous effects on turbulence, fine grid spacing is required near airfoil surface to resolve the viscous layer. These turbulence models are outlined as follows.

### Baldwin–Barth One-Equation Model

The turbulent viscosity in the B–B one-equation model[10] is modeled as

$$\tilde{\nu}_t = C_\mu \mathcal{D}_1 \mathcal{D}_2 \tilde{\nu}\tilde{R}_T \tag{3}$$

where $\tilde{\nu}$ is the kinematic viscosity and the turbulence field variable $\tilde{\nu}\tilde{R}_T$ is governed by the transport equation written in nondimensional form as

$$\frac{\mathrm{D}(\tilde{\nu}\tilde{R}_T)}{\mathrm{D}t} = \frac{\overline{\gamma} M_\infty}{\sqrt{Re_L}} \left[ \left( \tilde{\nu} + \frac{\tilde{\nu}_t}{\sigma_\epsilon} \right) \nabla^2 (\tilde{\nu}\tilde{R}_T) - \frac{1}{\sigma_\epsilon} \nabla \tilde{\nu}_t \cdot \nabla (\tilde{\nu}\tilde{R}_T) \right] + (C_{\epsilon_2} \mathcal{F}_\epsilon - C_{\epsilon_1}) \sqrt{\tilde{\nu}\tilde{R}_T}\, \mathcal{P} \tag{4}$$

where $\mathrm{D}/\mathrm{D}t$ is the substantive derivative, $\mathrm{D}/\mathrm{D}t = (\partial/\partial t) + \boldsymbol{V} \cdot \nabla$ and $\mathcal{P}$ is the production of the turbulent kinetic energy,

$$\mathcal{P} = \tilde{\nu}_t \left( \frac{\partial \tilde{V}_i}{\partial x_j} + \frac{\partial \tilde{V}_j}{\partial x_i} \right) \frac{\partial \tilde{V}_i}{\partial x_j} - \frac{2}{3} \tilde{\nu}_t \left( \frac{\partial \tilde{V}_k}{\partial x_k} \right)^2$$

The following functions are employed to account for near-wall viscous effects on turbulence:

$$\mathcal{F}_\epsilon(y^+) = \frac{C_{\epsilon_1}}{C_{\epsilon_2}} + \left( 1 - \frac{C_{\epsilon_1}}{C_{\epsilon_2}} \right) \left( \frac{1}{\kappa y^+} + \mathcal{D}_1 \mathcal{D}_2 \right) \times \left[ \sqrt{\mathcal{D}_1 \mathcal{D}_2} + \frac{y^+}{\sqrt{\mathcal{D}_1 \mathcal{D}_2}} (\mathcal{D}_1 \mathcal{D}_2 + \mathcal{D}_1 \mathcal{D}_2) \right]$$

$$\frac{1}{\sigma_\epsilon} = (C_{\epsilon_2} - C_{\epsilon_1}) \sqrt{\frac{C_\mu}{\kappa^2}}, \qquad y^+ = \sqrt{\frac{\tilde{\tau}_{\text{wall}}}{\langle \rho \rangle_{\text{wall}}}} \frac{\Delta y}{\tilde{\nu}}$$

$$\mathcal{D}_1 = 1 - \exp\left( \frac{-y^+}{A^+} \right), \qquad \mathcal{D}_2 = 1 - \exp\left( \frac{-y^+}{A_2^+} \right)$$

$$\mathcal{D}_1 = \frac{1}{A^+} \exp\left( \frac{-y^+}{A^+} \right), \qquad \mathcal{D}_2 = \frac{1}{A_2^+} \exp\left( \frac{-y^+}{A_2^+} \right)$$

where $\Delta y$ is the distance from the field point to the nearest wall and the modeling constants are given as $\kappa = 0.41$, $C_{\epsilon_1} = 1.2$, $C_{\epsilon_2} = 2.0$, $C_\mu = 0.09$, $A^+ = 26$, and $A_2^+ = 10$.

### Spalart–Allmaras One-Equation Model

In the S–A model,[11] the turbulent viscosity is given by

$$\tilde{\nu}_t = \tilde{\varphi} f_{v1} \tag{5}$$

where $f_{v1} = \chi^3/(\chi^3 + C_{v1}^3)$ and $\chi \equiv \tilde{\varphi}/\tilde{\nu}$. After neglecting the trip functions from the original model,[11] the transport equation of the turbulence field variable $\tilde{\varphi}$ is written as

$$\frac{\mathrm{D}\tilde{\varphi}}{\mathrm{D}t} = \frac{\overline{\gamma} M_\infty}{\sqrt{Re_L}} \left( \frac{1}{\sigma} \{ \nabla \cdot [(\tilde{\nu} + \tilde{\varphi}) \nabla \tilde{\varphi}] + C_{b2} (\nabla \tilde{\varphi})^2 \} - C_{w1} f_w \left[ \frac{\tilde{\varphi}}{d} \right]^2 \right) + C_{b1} \tilde{S} \tilde{\varphi} \tag{6}$$

where $\tilde{S} \equiv S + \tilde{\varphi} f_{v2}/(\kappa^2 d^2)$, $f_{v2} = 1 - \chi/(1 + \chi f_{v1})$, $f_\omega = g[(1 + C_{w3}^6)/(g^6 + C_{w3}^6)]^{1/6}$, $g = r + C_{w2}(r^6 - r)$, and $r \equiv \tilde{\varphi}/(\tilde{S}\kappa^2 d^2)$. Here $S$ is the magnitude of the vorticity and $d$ is the distance to the closest wall.

The model constants given by Spalart and Allmaras[11] are $\kappa = 0.41$, $C_{b1} = 0.1355$, $\sigma = \frac{2}{3}$, $C_{b2} = 0.622$, $C_{w1} = C_{b1}/\kappa^2 + (1 + C_{b2})/\sigma$, $C_{w2} = 0.3$, $C_{w3} = 2$, and $C_{v1} = 7.1$.

### Chien's Low Reynolds Number $k$–$\epsilon$ Model

In the CH low Reynolds number $k$–$\epsilon$ model,[12] the nondimensional turbulent viscosity is expressed by

$$\tilde{\nu}_t = (Re_L/\overline{\gamma} M_\infty) C_\mu \mathcal{F}_\mu (\tilde{k}^2/\tilde{\epsilon}) \tag{7}$$

where $\tilde{k} = \frac{1}{2}\langle \rho V_i'' V_i'' \rangle / \langle \rho \rangle$ is the turbulent kinetic energy and $\tilde{\epsilon} = \tilde{\nu} \langle \rho V_{i,j}'' V_{i,j}'' \rangle / \langle \rho \rangle$ is the isotropic dissipation rate of the turbulent kinetic energy.

The transport equations, which govern the turbulence field variables $\tilde{k}$ and $\tilde{\epsilon}$, are described by

$$\frac{\mathrm{D}\langle \boldsymbol{U}_{k\epsilon} \rangle}{\mathrm{D}t} = \frac{\overline{\gamma} M_\infty}{\sqrt{Re_L}} \left( \frac{\partial \langle \boldsymbol{R}_{k\epsilon} \rangle}{\partial x} + \frac{\partial \langle \boldsymbol{S}_{k\epsilon} \rangle}{\partial y} + \langle \boldsymbol{K}_{k\epsilon} \rangle \right) \tag{8}$$

where

$$\langle \boldsymbol{U}_{k\epsilon} \rangle = (\tilde{k}, \tilde{\epsilon})^T \qquad \langle \boldsymbol{R}_{k\epsilon} \rangle = \left[ \left( \tilde{\nu} + \frac{\tilde{\nu}_t}{\sigma_k} \right) \frac{\partial \tilde{k}}{\partial x}, \left( \tilde{\nu} + \frac{\tilde{\nu}_t}{\sigma_\epsilon} \right) \frac{\partial \tilde{\epsilon}}{\partial x} \right]^T$$

$$\langle \boldsymbol{S}_{k\epsilon} \rangle = \left[ \left( \tilde{\nu} + \frac{\tilde{\nu}_t}{\sigma_k} \right) \frac{\partial \tilde{k}}{\partial y}, \left( \tilde{\nu} + \frac{\tilde{\nu}_t}{\sigma_\epsilon} \right) \frac{\partial \tilde{\epsilon}}{\partial y} \right]^T$$

$$\langle \boldsymbol{K}_{k\epsilon} \rangle = \left[ \mathcal{P} - \frac{Re_L}{\overline{\gamma} M_\infty} \tilde{\epsilon} + \mathcal{E},\ \frac{\tilde{\epsilon}}{\tilde{k}} \left( C_1 \mathcal{P} - \frac{Re_L}{\overline{\gamma} M_\infty} \mathcal{F}_2 C_2 \tilde{\epsilon} \right) + \mathcal{E} \right]^T$$

Here the production of the turbulent kinetic energy

$$\mathcal{P} = \tilde{\nu}_t \left( \frac{\partial \tilde{V}_i}{\partial x_j} + \frac{\partial \tilde{V}_j}{\partial x_i} \right) \frac{\partial \tilde{V}_i}{\partial x_j} - \frac{2}{3} \tilde{\nu}_t \left( \frac{\partial \tilde{V}_k}{\partial x_k} \right)^2 - \frac{2}{3} \tilde{k} \frac{\partial \tilde{V}_k}{\partial x_k}$$

Chien[12] proposed the following functions for this model:

$$\mathcal{F}_1 = 1 - \exp(-0.0115 y^+), \qquad \mathcal{F}_2 = 1 - \frac{2}{9} \exp\left( -\frac{R_t^2}{36} \right)$$

$$R_t = \frac{Re_L}{\overline{\gamma} M_\infty} \frac{\tilde{k}^2}{\tilde{\nu}\tilde{\epsilon}}, \qquad \mathcal{E} = -\frac{2\tilde{\nu}\tilde{k}}{\Delta y^2}$$

$$\mathcal{E} = -\frac{2\tilde{\nu}\tilde{\epsilon}}{\Delta y^2} \exp(-0.5 y^+), \qquad y^+ = \sqrt{\frac{\tilde{\tau}_{\text{wall}}}{\langle \rho \rangle_{\text{wall}}}} \frac{\Delta y}{\tilde{\nu}}$$

The extra terms, $\mathcal{E}$ and $\mathcal{E}$, are used to account for near-wall viscous effects on turbulence. The model constants are $\sigma_k = 1.0$, $\sigma_\epsilon = 1.3$, $C_\mu = 0.09$, $C_1 = 1.35$, and $C_2 = 1.8$.

## IV. Solution Procedure

The basic strategy involved in this work is based on a decoupled approach with different solution procedures used for the mean flow equations and the turbulence closure equations. For the mean flow equations, the solution procedure uses a cell-centered finite volume spatial description with an explicit multistage time integration scheme to solve for steady-state solutions. In principle, the turbulence transport equations can be solved using the same explicit scheme. However the presence of source terms in the turbulence model equations and the positivity constraints of the turbulence quantities impose a further time step restriction. Hence, an implicit factored ADI scheme is used for solving the turbulence closure equations to alleviate this restriction.

### Explicit Finite Volume Multistage Time Integration of Mean Flow Equations

The mean flow equations governed by the Favre-averaged Navier–Stokes equations are discretized using a multistage cell-centered finite volume time-marching scheme as in Refs. 13 and 14. In the cell-centered finite volume formulation, the flow variables are stored at the cell centers with the control volume for each cell being defined by the surrounding grid points. The finite volume formulation results in a system of semidiscrete equations of the general form

$$\frac{\mathrm{d}(h\boldsymbol{U})_{i,j}}{\mathrm{d}t} + (\boldsymbol{Q}_c)_{i,j} + (\boldsymbol{Q}_v)_{i,j} = 0 \tag{9}$$

where $h_{i,j}$ is the area of the mesh cell indexed as $(i, j)$, which are indices along the two general coordinate directions along which the cell boundaries are aligned, and $\boldsymbol{Q}_c$ and $\boldsymbol{Q}_v$ are the net convective and viscous fluxes out of the cell boundaries, respectively. The convective fluxes are computed at the faces as the average of the flux vectors defined in the two adjacent cells. The face values of velocity and temperature gradients required in the viscous fluxes are computed by integrating the control volume defined by the two adjacent cell centers and the endpoints of the dividing face. Because the finite-volume spatial discretization used here is equivalent to a central difference scheme, additional artificial dissipation is required to suppress odd–even point decoupling. Adding artificial dissipative terms to Eq. (9) in a conservative form results in the final form of the finite volume spatial discretization,

$$\frac{\mathrm{d}(h\boldsymbol{U})_{i,j}}{\mathrm{d}t} + (\boldsymbol{Q}_c)_{i,j} + (\boldsymbol{Q}_v)_{i,j} - \boldsymbol{D}_{i,j} = 0 \tag{10}$$

where $\boldsymbol{D}_{i,j}$ is the net dissipation of the cell and is given by $\boldsymbol{D}_{i,j} = \boldsymbol{d}_{i+1/2,j} - \boldsymbol{d}_{i-1/2,j} + \boldsymbol{d}_{i,j+1/2} - \boldsymbol{d}_{i,j-1/2}$. The terms $\boldsymbol{d}_{i\pm1/2,j}$ and $\boldsymbol{d}_{i,j\pm1/2}$ indicate the dissipative terms in the $i$ and $j$ directions, respectively.

### CUSP Formulation

In the CUSP scheme proposed by Jameson,[6] the diffusive flux is defined as a combination of differences of the state and flux vectors. To help clarity, the diffusive flux for one coordinate, i.e., the $i$ direction, is described in detail as

$$\boldsymbol{d}_{i+\frac{1}{2}} = \tfrac{1}{2}\alpha^*_{i+\frac{1}{2}} c(\boldsymbol{U}_{i+1} - \boldsymbol{U}_i) + \tfrac{1}{2}\beta_{j+\frac{1}{2}}(\boldsymbol{F}_{i+1} - \boldsymbol{F}_i) \tag{11}$$

where $c$ is the speed of sound and the inviscid flux vector $\boldsymbol{F}$ is decomposed by setting

$$\boldsymbol{F} = \boldsymbol{U}u + \boldsymbol{P} \tag{12}$$

where $u$ is the velocity component in the $i$ direction. This formulation permits a solution with constant total enthalpy, $\rho h = \rho e + p$, by defining the state vector $\boldsymbol{U} = (\rho, \rho u, \rho v, \rho h)^T$ and $\boldsymbol{P} = p(0, 1, 0, 0)^T$, leading to the H-CUSP scheme. Then

$$\boldsymbol{F}_{i+1} - \boldsymbol{F}_i = \bar{u}(\boldsymbol{U}_{i+1} - \boldsymbol{U}_i) + \bar{\boldsymbol{U}}(u_{i+1} - u_i) + \boldsymbol{P}_{i+1} - \boldsymbol{P}_i \tag{13}$$

where $\bar{u}$ and $\bar{\boldsymbol{U}}$ are the arithmetic averages. If the total effective coefficient of convective diffusion is defined as

$$\alpha c = \alpha^* c + \beta\bar{u}$$

then the diffusive flux can be written as

$$\boldsymbol{d}_{i+\frac{1}{2}} = \tfrac{1}{2}\alpha c\Delta\boldsymbol{U} + \tfrac{1}{2}\beta\bar{\boldsymbol{U}}\Delta u + \tfrac{1}{2}\beta\Delta\boldsymbol{P} \tag{14}$$

and the diffusion coefficients are defined as

$$\alpha = |M|, \qquad \beta = \begin{cases} \max\left(0, \dfrac{u+\lambda^-}{u-\lambda^-}\right) & \text{if } 0 \le M \le 1 \\ \min\left(0, \dfrac{u+\lambda^+}{u-\lambda^+}\right) & \text{if } -1 \le M \le 0 \\ \operatorname{sign}(M) & \text{if } |M| \ge 1 \end{cases} \tag{15}$$

where $M = u/c$ is the Mach number and

$$\lambda^\pm = \frac{\gamma+1}{2\gamma}u \pm \sqrt{\left(\frac{\gamma+1}{2\gamma}u\right)^2 + \frac{c^2-u^2}{\gamma}}$$

Near stagnation points $\alpha$ may be modified to $\alpha = \frac{1}{2}(\alpha_0 + |M|^2/\alpha_0)$ if $|M|$ is smaller than a threshold $\alpha_0$. The interface variables involved in $\alpha$ and $\beta$ are computed using the Roe-averaged quantities defined as a density weighted average of the left and right states.[5]

A high-resolution scheme can be constructed by limiting the action of antidiffusive terms. In a similar manner to the reconstruction of the solution in van Leer's MUSCL scheme,[15] Jameson[6] defines left and right states for each dependent variable separately as

$$\boldsymbol{U}^{(k)}_L = \boldsymbol{U}^{(k)}_i + \tfrac{1}{2}L\left(\Delta\boldsymbol{U}^{(k)}_{i+\frac{3}{2}}, \Delta\boldsymbol{U}^{(k)}_{i-\frac{1}{2}}\right)$$

$$\boldsymbol{U}^{(k)}_R = \boldsymbol{U}^{(k)}_{i+1} - \tfrac{1}{2}L\left(\Delta\boldsymbol{U}^{(k)}_{i+\frac{3}{2}}, \Delta\boldsymbol{U}^{(k)}_{i-\frac{1}{2}}\right)$$

where $\boldsymbol{U}^{(k)}$ represent the $k$th element of the state vector $\boldsymbol{U}$ and

$$\Delta\boldsymbol{U}_{i+\frac{1}{2}} = \boldsymbol{U}_{i+1} - \boldsymbol{U}_i$$

The limited average $L(u, v)$ is defined as

$$L(u, v) = \tfrac{1}{2}D(u, v)(u + v) \tag{16}$$

where $D(u, v)$ is a factor that should deflate the arithmetic average and become zero if $u$ and $v$ have opposite signs. Take

$$D(u, v) = 1 - \left|\frac{u - v}{\max(|u| + |v|, \epsilon\Delta x^r)}\right|^q \tag{17}$$

In the CUSP scheme the pressures $p_L$ and $p_R$ for the left and right states are determined from $\boldsymbol{U}_L$ and $\boldsymbol{U}_R$, respectively. Then the diffusive flux is calculated by substituting $\boldsymbol{U}_L$ for $\boldsymbol{U}_i$ and $\boldsymbol{U}_R$ for $\boldsymbol{U}_{i+1}$ to give

$$\boldsymbol{d}_{i+\frac{1}{2}} = \tfrac{1}{2}\alpha^* c(\boldsymbol{U}_R - \boldsymbol{U}_L) + \tfrac{1}{2}\beta[\boldsymbol{F}(\boldsymbol{U}_R) - \boldsymbol{F}(\boldsymbol{U}_L)]$$

A similar expression for the diffusive terms in the $j$ direction can be derived. In the present work $q$ is taken as 3 with $r = \frac{3}{2}$ to ensure a second-order accuracy in smooth regions.

The semidiscretized mean flow equations are integrated in time using a multistage scheme in which the convective and dissipative terms are treated separately. The viscous fluxes ($\langle\boldsymbol{R}\rangle$, $\langle\boldsymbol{S}\rangle$) are only evaluated at the first stage and frozen for subsequent stages. For the results presented here, a five-stage scheme with dissipative terms reevaluated at alternate stages[6] is used. The convergence rate is enhanced through the use of local time stepping, implicit residual smoothing, and multigrid acceleration method in a manner similar to that discussed in Ref. 14. The multigrid cycle employed here is a saw-tooth cycle. On multigrid cycles, multistage time integration is done on each coarse mesh and the viscous fluxes are only updated on the first stage of the time stepping scheme on the finest mesh and frozen on coarser meshes. Once the coarsest mesh is reached, the solution changes are interpolated back to the finest mesh, with an additional multistage integration being performed on the way up.

### Implicit Factored ADI Formulation for Turbulence Closure Equations

To ensure positive turbulence quantities at each time step, the approach of Baldwin and Barth[10] for construction of $M$-type matrices is employed. An $M$-type matrix is diagonally dominant with positive diagonal entries and negative off-diagonal entries. The matrix has a nonnegative inverse operator; hence, the positivity of turbulence quantities is achieved. The turbulence model equations can be written in a general form as follows:

$$\frac{\partial \mathcal{R}}{\partial t} + \boldsymbol{V}\cdot\nabla\mathcal{R} = \nu_{t1}\nabla^2\mathcal{R} + \nabla\cdot(\nu_{t2}\nabla\mathcal{R}) + \boldsymbol{K} \tag{18}$$

where $\mathcal{R}$ is $\nu R_T$, $\varphi$, or $(k, \epsilon)^T$ and $\boldsymbol{K}$ represents the corresponding source terms for each model, which can be constructed from Eqs. (4), (6), and (8). The convective term is treated using a standard, first-order accurate upwind approximation,

$$\begin{aligned}\boldsymbol{V}\cdot\nabla\mathcal{R} \approx{}& \alpha_c^x\mathcal{R}_{i+1,j} + \beta_c^x\mathcal{R}_{ij} + \gamma_c^x\mathcal{R}_{i-1,j} \\ &+ \alpha_c^y\mathcal{R}_{i,j+1} + \beta_c^y\mathcal{R}_{ij} + \gamma_c^y\mathcal{R}_{i,j-1}\end{aligned} \tag{19}$$

where

$$\alpha_c^x = (1/\Delta x)u_{i,j}^-, \qquad \gamma_c^x = -(1/\Delta x)u_{i,j}^+, \qquad \beta_c^x = -(\alpha_c^x + \gamma_c^x)$$

$$\alpha_c^y = (1/\Delta y)v_{i,j}^-, \qquad \gamma_c^y = -(1/\Delta y)v_{i,j}^+, \qquad \beta_c^y = -(\alpha_c^y + \gamma_c^y)$$

and $u^\pm = (u \pm |u|)/2$ and $v^\pm = (v \pm |v|)/2$. Note that the matrix formed by $\alpha_c^x$, $\beta_c^x$, $\gamma_c^x$, $\alpha_c^y$, $\beta_c^y$, and $\gamma_c^y$ is an $M$-type matrix.

The diffusive terms are approximated by central differencing:

$$\begin{aligned}\nu_{t1}\nabla^2\mathcal{R} + \nabla\cdot(\nu_{t2}\nabla\mathcal{R}) \approx{}& \alpha^x\mathcal{R}_{i+1,j} + \beta^x\mathcal{R}_{ij} \\ &+ \gamma^x\mathcal{R}_{i-1,j} + \alpha^y\mathcal{R}_{i,j+1} + \beta^y\mathcal{R}_{ij} + \gamma^y\mathcal{R}_{i,j-1}\end{aligned} \tag{20}$$

To produce an $M$-type matrix, the entries are taken as

$$\begin{aligned}\alpha^\xi &= \max(0, \alpha_{d1}^\xi + \alpha_{d2}^\xi), \qquad \gamma^\xi = \max(0, \gamma_{d1}^\xi + \gamma_{d2}^\xi) \\ \beta^\xi &= -(\alpha^\xi + \gamma^\xi), \qquad \xi = x \quad \text{or} \quad y\end{aligned} \tag{21}$$

where

$$\alpha_{d1}^x = \gamma_{d1}^x = (1/\Delta x^2)(\nu_{t1})_{i,j}, \qquad \alpha_{d1}^y = \gamma_{d1}^y = (1/\Delta y^2)(\nu_{t1})_{i,j}$$

$$\alpha_{d2}^x = (1/\Delta x^2)(\nu_{t2})_{i+\frac{1}{2},j}, \qquad \gamma_{d2}^x = (1/\Delta x^2)(\nu_{t2})_{i-\frac{1}{2},j}$$

$$\alpha_{d2}^y = (1/\Delta y^2)(\nu_{t2})_{i,j+\frac{1}{2}}, \qquad \gamma_{d2}^y = (1/\Delta y^2)(\nu_{t2})_{i,j-\frac{1}{2}}$$

The source term $\boldsymbol{K}$ is treated explicitly. This results in a system of ordinary differential equations of the form

$$\frac{\mathrm{d}\mathcal{R}}{\mathrm{d}t} + M(\mathcal{R})\mathcal{R} = \boldsymbol{K}(\mathcal{R}) \tag{22}$$

or

$$[I + \Delta t M(\mathcal{R}^n)]\Delta\mathcal{R}^n = \boldsymbol{F}(\mathcal{R}^n)$$

where $\boldsymbol{F}(\mathcal{R}^n) = \Delta t[-M(\mathcal{R}^n)\mathcal{R}^n + \boldsymbol{K}(\mathcal{R}^n)]$. The resulting matrix $M$ is an $M$-type matrix that has a nonnegative inverse operator; hence, the positivity of turbulence quantities is achieved. The direct inversion of the matrix is time consuming. Therefore, it is further approximately factorized in the $x$ and $y$ directions to alleviate the problem:

$$[I + \Delta t M_x(\mathcal{R}^n)][I + \Delta t M_y(\mathcal{R}^n)]\Delta\mathcal{R}^n = \boldsymbol{F}(\mathcal{R}^n) \tag{23}$$

The two resulting matrices are tridiagonal for the one-equation model or $2 \times 2$ block tridiagonal for the two-equation model and can be easily inverted by utilizing Thomas' algorithm.[18] However, the $M$-type matrix is lost after factorization. In this work, $\Delta t$ is restricted to achieve the positivity.

### Boundary Conditions

The mean flow and turbulence transport equations presented in the preceding sections represent an initial-boundary-value problem. To solve these equations, it is necessary to impose initial and boundary conditions. Because only steady-state solutions are of interest in the present work, initial conditions are not relevant to the solutions. For two-dimensional mean flow equations, four boundary conditions are required along each boundary of the domain. The boundaries involved are either inflow/outflow or solid wall type. Along solid wall boundaries, the no-slip condition, zero normal pressure gradient, and adiabatic wall condition are specified.

For the two-dimensional airfoil problem, the inflow/outflow boundary is the far-field boundary placed at a finite extent. For subsonic flows, the nonreflecting boundary conditions based on the Riemann invariants of the one-dimensional inviscid flow normal to the far-field boundary are used. In addition to the Riemann invariants, on the inflow values of the tangential velocity, components and the entropy are determined using freestream values, whereas on the outflow those are extrapolated from the interior. Far-field boundaries are placed at a distance of 10 airfoil chord lengths from the airfoil. To accurately approximate the asymptotic state of a uniform freestream condition, the vortex far-field boundary condition,[16] which is defined as the combination of freestream and a compressible point vortex centered at the airfoil quarter chord, is used.

When a turbulence model based on differential equations of turbulence quantities is used, it requires additional boundary conditions for each equation. The boundary conditions are determined by the type of turbulence model used. Following Refs. 10–12, on solid walls $\mathcal{R} = 0$, on inflow boundaries $\mathcal{R} = \mathcal{R}_\infty$ and on outflow boundaries, $\mathcal{R}$ is extrapolated from the interior values. In this work, $R_{T\infty}$ and $\varphi_\infty$ are set to 0.1 and $0.01\nu_\infty$ respectively. The values of $k_\infty$ and $\epsilon_\infty$ are based on the specified freestream turbulence intensity and eddy viscosity, which are set as 0.1% and $0.1\nu_\infty$ respectively.

## V. Results

To verify the single-point shock capturing characteristics of the H-CUSP scheme, computations are first performed for transonic inviscid flow over the NACA-0012 airfoil configuration. Then some sample computations of compressible turbulent flow on a flat plate are done to validate the implicit factored ADI formulation of turbulence models. Finally, the high-resolution scheme is applied to turbulent transonic flow around the RAE-2822 airfoil to demonstrate the capability of the scheme in resolving complex flow structures, as well as to compare the performance of various turbulence models.

### Inviscid Transonic Flows Past Airfoils

To demonstrate the H-CUSP formulation, computations are performed on two C-type meshes of $192 \times 32$ and $384 \times 64$ cells for the inviscid transonic airfoil flows. The coarse mesh is obtained from the fine mesh by dropping every alternate grid line in both coordinate directions, while leaving the boundaries intact. Solutions are produced after 500 cycles of four multigrid levels. The computation considered is the NACA-0012 airfoil operating at a freestream Mach number of 0.8 and 0-deg angle of attack. This is a symmetric flow case with strong shocks at $x/c = 0.5$ on the upper and lower surfaces. For this nonlifting airfoil case, the upstream boundary is placed at a distance of 40 airfoil chord lengths from the airfoil to accurately approximate the uniform freestream conditions. The computed surface pressure coefficient distributions for the two meshes are shown in Fig. 1, in which the symmetry of the flow and the single-point shock capturing characteristics are clearly demonstrated. Figure 2 compares the convergence histories of $192 \times 32$ solution and $384 \times 64$ solutions. The convergence rate is about the same on the two meshes at the first few hundred cycles, but slightly slower for later cycles on the fine mesh. The number of supersonic points in the flowfield normalized by the number attained at the end of converged steady solution, NSUP, converges after about 250 multigrid cycles registering a more than four-order reduction of the root mean square (rms) value of the density residual, $\|\mathrm{d}\rho/\mathrm{d}t\|_2$, after 250 multigrid cycles.

### Compressible Turbulent Boundary Layer on a Flat Plate

The flat plate flow case is a standard test case for the validation of turbulent flow calculations. Because all of the turbulence models

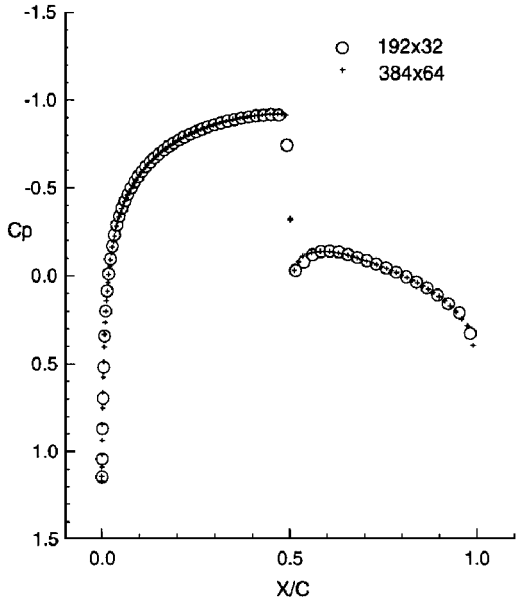


**Fig. 1 Computed surface pressure coefficient distributions for NACA-0012 airfoil at Mach 0.800 and $\alpha = 0.00$ deg.**

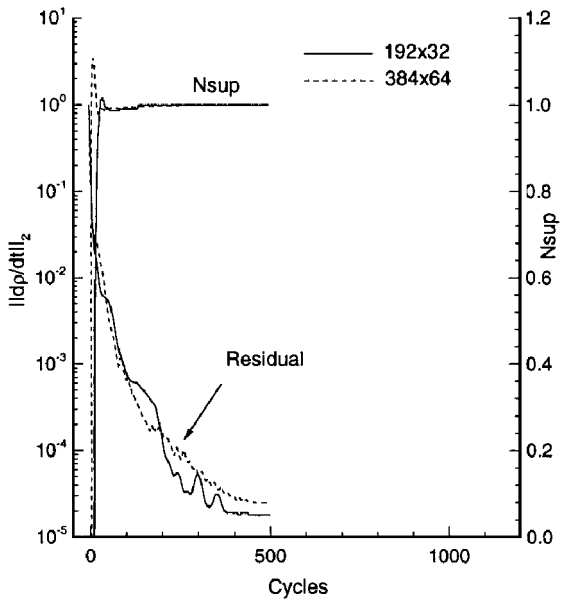


**Fig. 2 Convergence and number of supersonic points for NACA-0012 airfoil at Mach 0.800 and $\alpha = 0.00$ deg.**

are calibrated using the flat plate solution, an accurate prediction of this flow problem indicates a correct implementation of the turbulence model equations. The mesh employed to compute the turbulent boundary layer over flat plate consists of $72 \times 80$ mesh cells with 48 cells placed on the plate. It is algebraically packed near the leading edge of the plate and solid surface with minimum increments of $\Delta x_{\min} = 3 \times 10^{-4}$ and $\Delta y_{\min} = 3 \times 10^{-6}$ of plate length. The maximum aspect ratio of this mesh is about 40,000. The inlet boundary is placed at one-half of the plate length from the leading edge, and the exit boundary is located at the end of the plate. The upper boundary is set at one-tenth of the plate length above the plate.

The inflow and outflow boundary conditions are based on the characteristic boundary conditions with freestream static pressure prescribed along the exit boundary. Flow tangency is enforced along the symmetric boundary, which lies along the lower boundary upstream of the plate. A no-slip condition with an adiabatic wall and zero normal pressure gradient are imposed along the solid wall. At the upper boundary, the normal velocity component is extrapolated from the interior and other variables are specified as freestream. The present computations are performed for a freestream Mach number

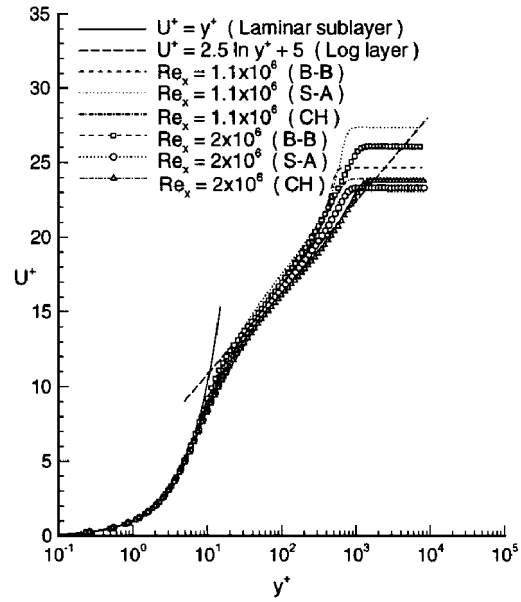


**Fig. 3 Comparison of the law of the wall profile for flat plate turbulent boundary layer.**

of 0.5 and a Reynolds number of $2.2 \times 10^6$ based on the plate length. Solutions are obtained in 2500 cycles of three multigrid levels, which reduces the rms of the density residuals by about four orders of magnitude. The velocity profiles computed using the three turbulence models are shown in Fig. 3 for $x = 0.5$ and 0.9. The agreement between the computed results and the logarithmic law of wall profile is excellent for all three models. The results at the two streamwise locations also illustrate the self-similarity law of the velocity profile.

### Turbulent Transonic Flow Past Airfoils

Turbulent transonic flow past a RAE-2822 airfoil inclined at an angle of attack of $\alpha = 2.92$ deg in a freestream Mach number $M_\infty = 0.725$ and Reynolds number $Re_L = 6.5 \times 10^6$, which is test case 6 in the experimental study of Cook et al.,[17] is used to validate the present study. To account for wall interference, corrected flow conditions suggested by Tatsumi et al.,[5] i.e., $M_\infty = 0.731$ and $\alpha = 2.51$ deg, are used in the study. This flow involves a strong shock wave at $x/c = 0.55$ on the upper surface. As the lift coefficient for this case depends on the predicted shock location, it is imperative that a good resolution of the shock be used for the calculation. A grid convergence study is performed on C-grids having $384 \times 64$ cells and $192 \times 32$ cells in the wraparound direction and the normal direction, respectively. Two-thirds of the wraparound cells lie on the airfoil surface and are packed to resolve the boundary layers. The minimum normal distances between the first grid lines off the airfoil surface, i.e., $(\Delta y_w)$, are $1 \times 10^{-5}$ and $2.2 \times 10^{-5}$ chords, respectively, for the two grids.

A grid convergence study is first presented for the three turbulence models within the H-CUSP scheme. Figure 4 compares the computed airfoil surface pressure coefficient and skin-friction coefficient distributions. The airfoil surface pressure distributions for all three models are in close agreement for most of the airfoil surface, with the fine grid solutions agreeing more closely with experimental data. The skin-friction distributions are in close agreement for most points on the airfoil surface for the two one-equation models, with the fine grid solutions capturing more details near shocks as expected. However, there are significant deviations in the skin-friction distributions for most points on the airfoil surface for the case of the CH low Reynolds number $k\_\epsilon$ model. It is felt that the deviations could be due to the values of $\Delta y_w$. To assess this, the two grids are refined further so that the $\Delta y_w$ for the $384 \times 64$ mesh is now $5 \times 10^{-6}$ chords and that for the $192 \times 32$ mesh is $1.1 \times 10^{-5}$ chords. Figure 5 compares the airfoil surface pressure coefficient and skin-friction coefficient distributions for different normal wall

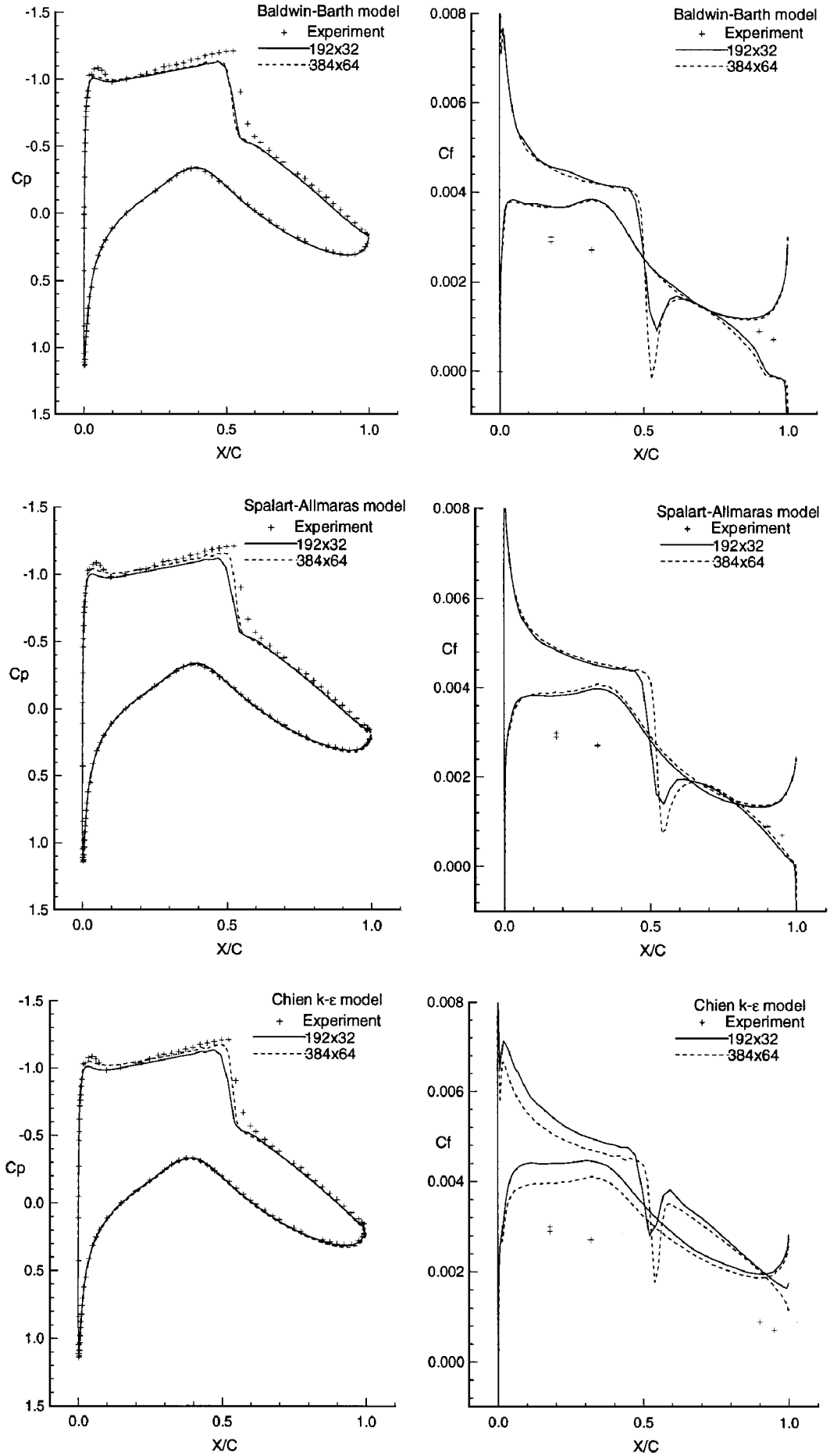


**Fig. 4 Grid convergence study on surface pressure coefficient and skin-friction coefficient distributions using H-CUSP scheme with three turbulence models for RAE-2822 airfoil at Mach 0.731, $\alpha = 2.51$ deg, and $Re_L = 6.5 \times 10^6$.**

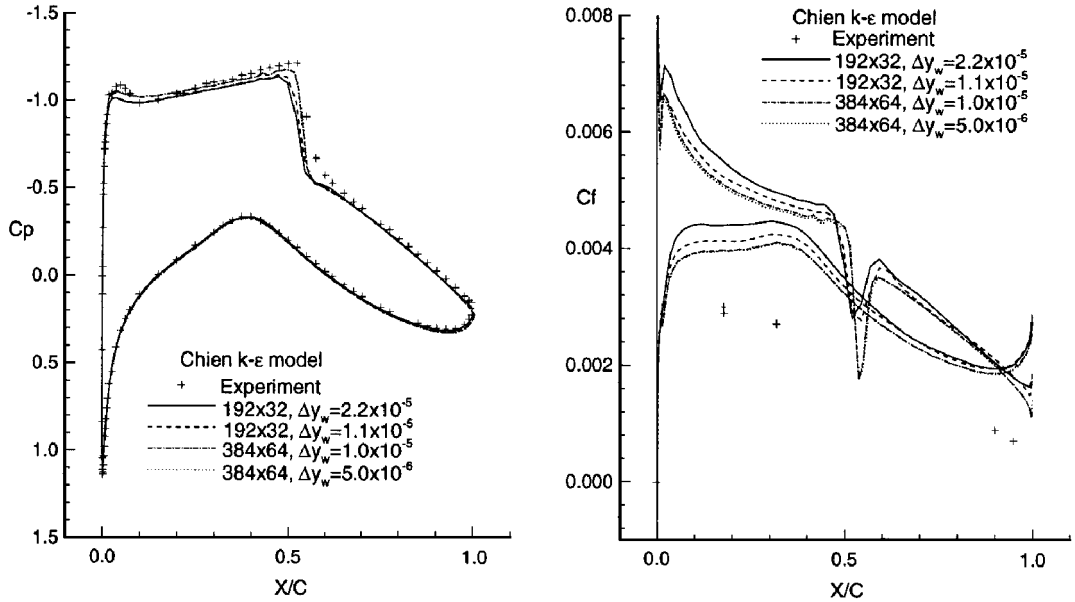


**Fig. 5 Mesh convergence study on surface pressure coefficient and skin-friction coefficient distributions using H-CUSP scheme with CH $k$–$\epsilon$ model for RAE-2822 airfoil at Mach 0.731, $\alpha = 2.51$ deg, and $Re_L = 6.5 \times 10^6$.**

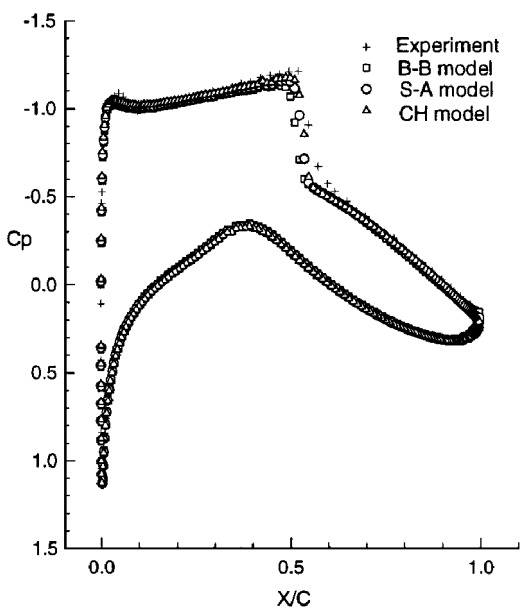


**Fig. 6 Comparison of surface pressure coefficient distributions on 384 × 64 mesh using H-CUSP scheme with three turbulence models for RAE-2822 airfoil at Mach 0.731, $\alpha = 2.51$ deg, and $Re_L = 6.5 \times 10^6$.**

spacings, and it can be seen that when finer values of $\Delta y_w$ are imposed on the grids closer agreement is achieved for most points on the airfoil surface. It seems that grid independent solutions using the CH low Reynolds number $k$–$\epsilon$ model are more sensitive to $\Delta y_w$ and its variation near the wall than those solutions using the one-equation turbulence models.

Figure 6 shows the comparison of surface pressure coefficient distributions with the experimental data for the three turbulence models on the 384 × 64 mesh with $\Delta y_w = 1.0 \times 10^{-5}$ chords. The computed results are in close agreement with the experimental data. Computed lift and drag coefficients are ($C_L = 0.691$ and $C_D = 0.0134$), ($C_L = 0.715$ and $C_D = 0.0145$), and ($C_L = 0.731$ and $C_D = 0.0160$) for the B–B, S–A, and CH models, respectively.

The experimental values given by Cook et al.[17] are ($C_L = 0.743$ and $C_D = 0.0127$). To study the resolution characteristics of the H-CUSP and standard scalar dissipation models, computed results are also presented for the two dissipation models using the B–B one-equation model on the 384 × 64 mesh with $\Delta y_w = 1.0 \times 10^{-5}$. Figures 7a and 7b show contour plots of the computed field Mach

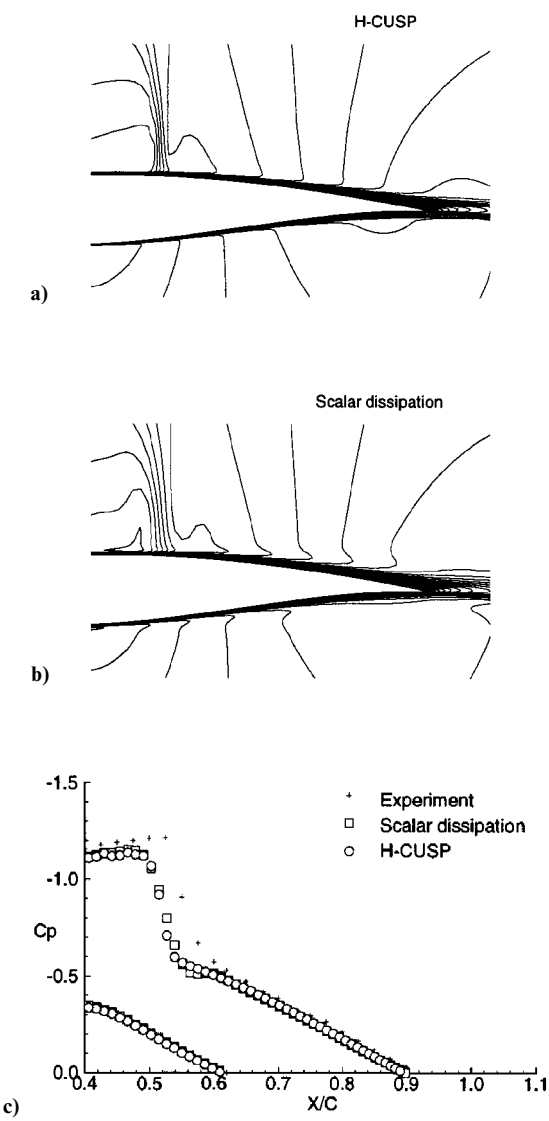


**Fig. 7 Comparison of surface pressure coefficient distributions and Mach number contours on 384 × 64 mesh using scalar dissipation and H-CUSP schemes for RAE-2822 airfoil at Mach 0.731, $\alpha = 2.51$ deg, and $Re_L = 6.5 \times 10^6$.**

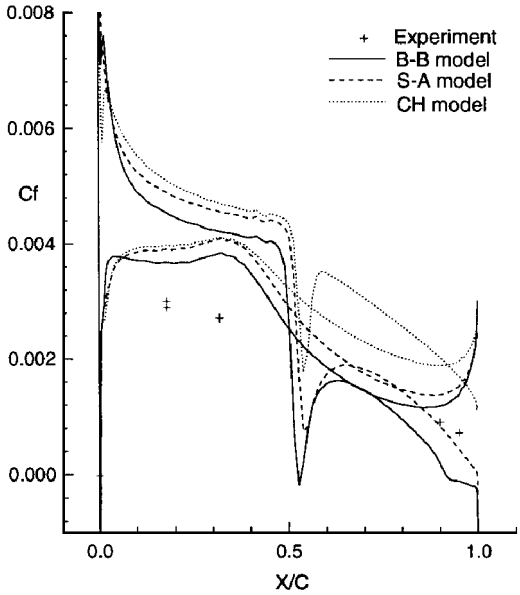


**Fig. 8 Comparison of skin-friction coefficient distributions on 384 × 64 mesh using H-CUSP scheme with three turbulence models for RAE-2822 airfoil at Mach 0.731, $\alpha$ = 2.51 deg, and $Re_L = 6.5 \times 10^6$.**

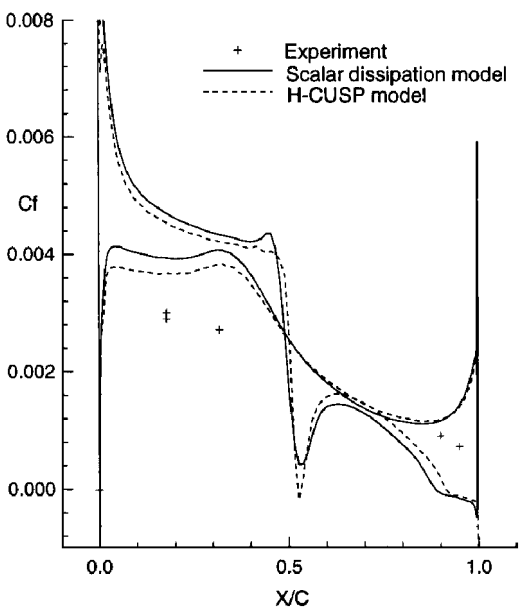


**Fig. 9 Comparison of skin-friction coefficient distributions on 384 × 64 mesh using scalar dissipation and H-CUSP schemes for RAE-2822 airfoil at Mach 0.731, $\alpha$ = 2.51 deg, and $Re_L = 6.5 \times 10^6$.**

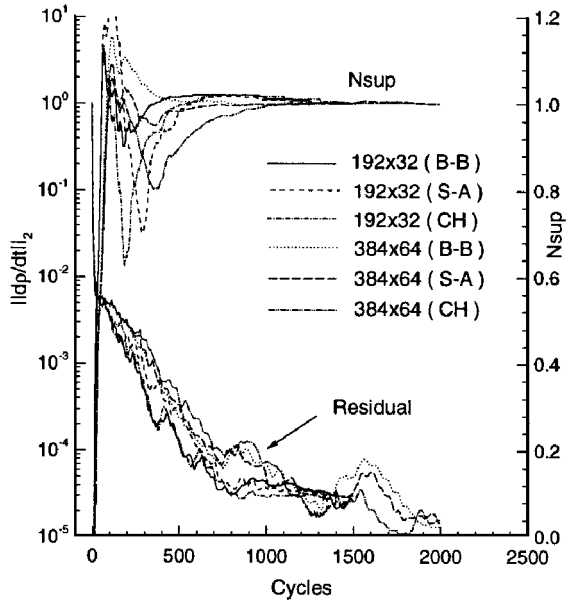


**Fig. 10 Convergence and number of supersonic point for RAE-2822 airfoil at Mach 0.731, $\alpha$ = 2.51 deg, and $Re_L = 6.5 \times 10^6$.**

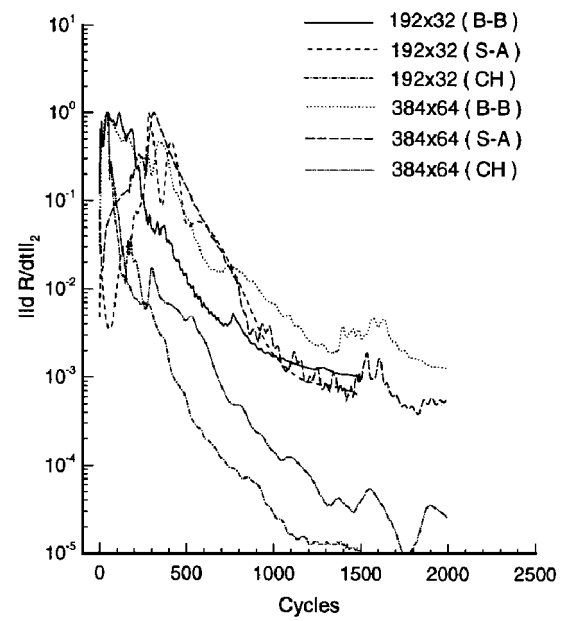


**Fig. 11 Convergence of turbulence transport equations for RAE-2822 airfoil at Mach 0.731, $\alpha$ = 2.51 deg, and $Re_L = 6.5 \times 10^6$.**

number distribution in the vicinity of the shock and viscous layers on the surface of the airfoil using the H-CUSP and standard scalar dissipation models. Figures 7a and 7b demonstrate the nonoscillatory character of the H-CUSP solution in the vicinity of the shock and its ability to resolve the structure of the flow discontinuities more crisply than the scalar dissipation model. Figure 7c shows a comparison of the airfoil surface pressure coefficient distribution in the vicinity of the shock wave for the two formulations of the dissipation models.

Figure 8 shows the comparison of computed skin-friction coefficient distributions, $C_f$, with the upper surface experimental data for the three turbulence models. It is difficult to assess the performance of the three models on $C_f$ because only limited experimental data are available. However, all three models predict fair agreement qualitatively with the available experimental data. Computed results using the three models are in good agreement with each other except on the region downstream from the shock where the CH model predicts a slightly higher $C_f$ than the other two models do. In addition, computed results of the B–B model shows reversed flows near the trailing-edge region. Figure 9 shows the comparison of skin-friction coefficient distributions for scalar and H-CUSP solutions using the B–B model. The slight change between the two computed results is due to the different resolution characteristics of the two artificial dissipation models. The difference may be seen as an indication of the improvement of the H-CUSP solutions over the scalar dissipation solutions. Convergence histories are shown in Figs. 10 and 11 for the rms residuals $\|\mathrm{d}\tilde{\rho}/\mathrm{d}t\|_2$ and $\|\mathrm{d}\tilde{R}/\mathrm{d}t\|_2$, respectively. The same convergence rate of $\|\mathrm{d}\tilde{\rho}/\mathrm{d}t\|_2$ is observed for the three turbulence models. The rms of the density residual drops by about five orders of magnitude after 1500 and 2000 cycles using three levels of multigrid for the 192 × 32 and 384 × 64 meshes, respectively.

## VI. Conclusion

A high-resolution finite volume scheme has been demonstrated with solution of various two-dimensional inviscid and turbulent transonic flows. In the case presented, an improved resolution of shock wave and viscous layer is described through the use of the

high-resolution scheme. It has been found that the high-resolution scheme can handle different turbulent flow features, provided the turbulence models used are capable of accurately resolving turbulence effects on the mean flow equations. For the computation of turbulence effects on the mean flows, three turbulence models are used, B–B one-equation, S–A one-equation, and CH low Reynolds number $k$–$\epsilon$ models. Computed solutions of all three models are in good agreement with experimental data for the investigated test case. In addition, the mesh convergence study shows that the CH $k$–$\epsilon$ model is more sensitive to the minimum normal wall spacing and near-wall mesh variation than the B–B and S–A one-equation models.

## Acknowledgment

The first author acknowledges the National Science and Technology Board, Singapore, for their support of his postdoctoral fellowship at Nanyang Technological University (NTU). Computing facilities at the National Supercomputing Research Centre, Singapore, and the Centre for Graphics and Imaging Technology, NTU, were used to obtain the results.

## References

[1]Kunz, R., "Explicit Navier–Stokes Computation of Turbomachinery Flowfields," Ph.D. Dissertation, Dept. of Aerospace Engineering, Pennsylvania State Univ., State College, PA, Aug. 1991.

[2]Varma, R. R., and Caughey, D. A., "Evaluation of Navier–Stokes Solutions Using Integrated Effect of Numerical Dissipation," AIAA Paper 93-0539, Jan. 1993.

[3]Turkel, E., and Vatsa, V. N., "Effect of Artificial Viscosity on Three-Dimensional Flow Solutions," *AIAA Journal*, Vol. 32, No. 1, 1994, pp. 39–45.

[4]Jameson, A., "Artificial Diffusion, Upwind Biasing, Limiters and Their Effect on Accuracy and Multigrid Convergence in Transonic and Hypersonic Flow," AIAA Paper 93-3359, July 1993.

[5]Tatsumi, S., Martinelli, L., and Jameson, A., "A New High Resolution Scheme for Compressible Viscous Flow with Shocks," AIAA Paper 95-0466, Jan. 1995.

[6]Jameson, A., "Positive Schemes and Shock Modelling for Compressible Flow," *International Journal for Numerical Methods in Fluids*, Vol. 20, No. 8/9, 1995, pp. 743–776.

[7]Damodaran, M., and Lee, K. H., "Finite Volume Calculation of Steady Viscous Compressible Flows Past Airfoils," *Journal of Institution of Engineers, Singapore*, Vol. 33, No. 5, 1993, pp. 39–44.

[8]Favre, A., "Équations des gaz Turbulents Compressibles I," *Journal des Mecanique*, Vol. 4, No. 3, 1965, pp. 361–390.

[9]Favre, A., "Équations des gaz Turbulents Compressibles II," *Journal des Mecanique*, Vol. 4, No. 4, 1965, pp. 391–421.

[10]Baldwin, B. S., and Barth, T. J., "A One-Equation Turbulence Transport Model for High Reynolds Number Wall-Bounded Flows," AIAA Paper 91-0610, Jan. 1991.

[11]Spalart, P. R., and Allmaras, S. R., "A One-Equation Turbulence Model for Aerodynamics Flows," AIAA Paper 92-0439, Jan. 1992.

[12]Chien, K. Y., "Predictions of Channel and Boundary-Layer Flows with a Low-Reynolds-Number Turbulence Model," *AIAA Journal*, Vol. 20, No. 1, 1982, pp. 33–38.

[13]Jameson, A., Schmidt, W., and Turkel, E., "Numerical Solution of the Euler Equations by Finite Volume Methods Using Runge–Kutta Time-Stepping Schemes," AIAA Paper 81-1259, June 1981.

[14]Martinelli, L., "Calculations of Viscous Flows with a Multigrid Method," Ph.D. Dissertation, Dept. of Mechanical and Aerospace Engineering, Princeton Univ., Princeton, NJ, Oct. 1987.

[15]Van Lee, B., "Towards the Ultimate Conservative Differencing Scheme. V. A Second Order Sequel to Godunov's Method," *Journal of Computational Physics*, Vol. 32, 1979, pp. 101–136.

[16]Usab, W. J., Jr., "Embedded Mesh Solutions of the Euler Equations Using a Multiple-Grid Method," Ph.D. Dissertation, Dept. of Aeronautics and Astronautics, Massachusetts Inst. of Technology, Cambridge, MA, Dec. 1983.

[17]Cook, T. J., McDonald, M. A., and Firmin, M. C. P., "Airfoil RAE 2822 Pressure Distributions and Boundary Layer and Wake Measurements," AGARD Advisory Rept. 138, May 1979, Sec. A6.

[18]Ferziger, J. H., and Peric, M., *Computational Methods for Fluid Dynamics*, Springer–Verlag, Berlin, 1996.

J. Kallinderis
*Associate Editor*